TO APPEAR IN *The Astrophysical Journal*.
Preprint typeset using LaTeX style emulateapj v. 5/2/11

arXiv:1602.01922v1 [astro-ph.GA] 5 Feb 2016

SUPERMASSIVE BLACK HOLES WITH HIGH ACCRETION RATES IN ACTIVE GALACTIC NUCLEI. VI. VELOCITY-RESOLVED REVERBERATION MAPPING OF Hβ LINE

PU DU[1,*], KAI-XING LU[2,1], CHEN HU[1], JIE QIU[1], YAN-RONG LI[1], YING-KE HUANG[1], FANG WANG[6], JIN-MING BAI[6], WEI-HAO BIAN[8], YE-FEI YUAN[9], LUIS C. HO[4,5] AND JIAN-MIN WANG[1,3,*]
(SEAMBH COLLABORATION)

Received 2015 December 22; accepted 2016 February 3

ABSTRACT

In the sixth of the series of papers reporting on a large reverberation mapping (RM) campaign of active galactic nuclei (AGNs) with high accretion rates, we present velocity-resolved time lags of Hβ emission lines for nine objects observed in the campaign during 2012–2013. In order to correct the line-broadening caused by seeing and instruments before the analysis of velocity-resolved RM, we adopt Richardson-Lucy deconvolution to reconstruct their Hβ profiles. The validity and effectiveness of the deconvolution are checked out by Monte Carlo simulation. Five among the nine objects show clear dependence of time delay on velocity. Mrk 335 and Mrk 486 show signatures of gas inflow whereas the clouds in the broad-line regions (BLRs) of Mrk 142 and MCG +06-26-012 tend to be radial outflowing. Mrk 1044 is consistent with the case of virialized motions. The lags of the rest four are not velocity-resolvable. The velocity-resolved RM of super-Eddington accreting massive black holes (SEAMBHs) shows that they have diversity of the kinematics in their BLRs. Comparing with the AGNs with sub-Eddington accretion rates, we do not find significant differences in the BLR kinematics of SEAMBHs.

Subject headings: accretion, accretion disks – galaxies: active – quasars: supermassive black holes

1. INTRODUCTION

Active galactic nuclei (AGNs) are very energetic sources powered by accretion onto supermassive black holes (SMBHs) in centers of their host galaxies. In optical/ultraviolet (UV) spectra of AGNs, the most prominent features are plenty of broad emission lines whose full-width-half-maximum (FWHM) spans from $\sim 10^3$ to 2×10^4 km s^{-1}(e.g., Schmidt 1963; Osterbrock & Mathews 1986; Boroson & Green 1992; Sulentic et al. 2000; Shen et al. 2011 and references therein). These emission lines originate from the gas in the broad-line regions (BLRs), which is photoionized by the continuum from central engines (Osterbrock 1989; Ho 2004). In the past decades, reverberation mapping (RM, e.g., Bahcall et al. 1972; Blandford & McKee 1982; Peterson et al. 1993) has become the mainstay in studying the kinematics and geometry of BLRs, as well as in measuring the masses of SMBHs in the centers of AGNs. It discerns the BLRs in time domain, instead of spatially, by monitoring spectroscopically the response of broad emission lines to the variations of continuum fluxes. RM observation has been carried out for more than 50 AGNs by many different groups (Peterson et al. 1993, 1998; Kaspi et al. 2000; Peterson et al. 2002, 2004; Kaspi et al. 2007; Bentz et al. 2008, 2009b; Denney et al. 2009a; Rafter et al. 2011, 2013; Barth et al. 2011, 2013, 2015; Du et al. 2014; Wang et al. 2014; Du et al. 2015; Shen et al. 2015), and measures successfully their time delays between the variations of continuum and emission lines. Enormous progress has been made in understanding the BLRs through RM observations (see recent reviews, e.g., Gaskell 2009; Popović 2012; Netzer 2013).

However, a main objective of RM is to reconstruct the so-called velocity-delay map (also known as "transfer function"), which is a function of the time lag and line-of-sight velocity of BLR gas, instead of only getting an averaged time lag of the emission line (Blandford & McKee 1982; Horne 1994; Horne et al. 2004). Due to the requirements of homogeneous sampling, accurate calibration, excellent signal-to-noise (S/N) ratios and high resolution for the reconstruction of velocity-delay maps (Horne et al. 2004), a relatively simpler analysis, that measuring the time lags of emission line as a function of line-of-sight velocity (velocity-resolved time lags), have been applied to about a dozen of AGNs (e.g., Bentz et al. 2008, 2009b, 2010; Denney et al. 2009a, 2010; Grier et al. 2013) and reveal the kinematics and geometry of their BLRs. It is very similar to the projection of velocity-delay map on the velocity axis. Furthermore, some more recent works have recovered the velocity-delay maps in several AGNs successfully by maximum entropy methods (Bentz et al. 2010; Grier et al. 2013) or Markov Chain Monte Carlo method (Pancoast et al. 2012, 2014b).

Since 2012, we have started a large RM campaign to monitor a sample of AGNs with high accretion rates, especially super-Eddington accreting massive black holes (SEAMBHs). The goal of the campaign is to understand better the super-Eddington accretion onto black holes, the BLR physics and their potential as a new probe of cosmological distance (Wang et al. 2013, 2014). The observations and light

[1] Key Laboratory for Particle Astrophysics, Institute of High Energy Physics, Chinese Academy of Sciences, 19B Yuquan Road, Beijing 100049, China
[2] Astronomy Department, Beijing Normal University, Beijing 100875, China
[3] National Astronomical Observatories of China, Chinese Academy of Sciences, 20A Datun Road, Beijing 100020, China
[4] Kavli Institute for Astronomy and Astrophysics, Peking University, Beijing 100871, China
[5] Department of Astronomy, School of Physics, Peking University, Beijing 100871, China
[6] Yunnan Observatories, Chinese Academy of Sciences, Kunming 650011, China
[8] Physics Department, Nanjing Normal University, Nanjing 210097, China
[9] Department of Astronomy, University of Science and Technology of China, Hefei 230026, China
[*] Corresponding author: (dupu,wangjm)@ihep.ac.cn

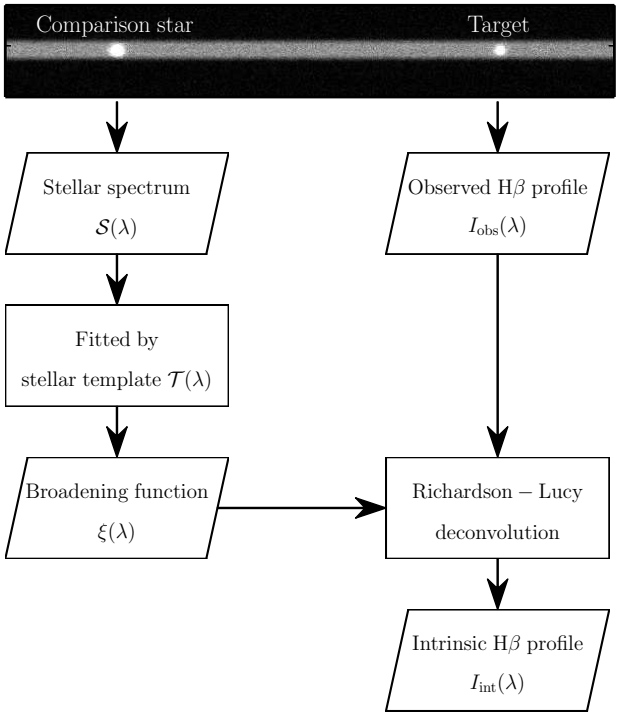

Figure 1. Flow chart of correction for line-broadening.

curves of Hβ emission line in the first year (2012-2013) have been published in Du et al. (2014, hereafter Paper I) and Wang et al. (2014, hereafter Paper II), and the time lags of their Fe II emission are presented in Hu et al. (2015, hereafter Paper III). The second stage of the campaign (2013-2014) have also been published in Du et al. (2015, hereafter Paper IV). These samples provide us opportunity to take a close look at the kinematics and geometry of the BLRs in high accretion rate AGNs. In particular, the well-known BLR radius-luminosity correlation ($R_{\rm BLR}-L_{5100}$ relationship, see Kaspi et al. 2000; Bentz et al. 2013) is reported to show some dependence on accretion rate (paper IV), implying that the BLRs are indeed different in AGNs with high accretion rates from the normal ones.

This paper presents the velocity-resolved time lags of the sources in the first year of our SEAMBH campaign. Section 2 gives a short review of the observation and data reduction. Section 3 describes in detail the deconvolution method we used to correct line-broadening caused by seeing and instruments, as well as a Monte Carlo simulation to evaluate the effectiveness of the correction. In this section, we also show a comparison of the Hβ profiles before and after the deconvolution procedures. The obtained velocity-resolved time lags are provided in Section 4. Section 5 gives a brief discussion and Section 6 a summary of the new results.

2. OBSERVATIONS AND DATA REDUCTION

Details of the target selection, the instruments, the observation and the procedures of data reduction of the campaign in 2012-2013 (hereafter SEAMBH2012) have been presented by Paper I and II. For completeness, in this section, we provide a brief summary of the main points.

2.1. *Sample Selection*

The targets selected for SEAMBH2012 are mainly narrow-line Seyfert 1 galaxies (NLS1s, see, e.g., Osterbrock & Pogge 1985), which, as a peculiar group of AGNs, are suspected to be candidates of SEAMBHs. The characteristics of NLS1s are: 1) narrow Balmer lines (FWHM $\lesssim$ 2000 km s^{-1}), 2) strong optical Fe II emission (relative to Hβ), 3) weak [O III] lines and 4) steep hard X-ray spectrum (Osterbrock & Pogge 1985; Boller et al. 1996). We selected NLS1s with extremely steep 2–10 keV continuum, which is known to anti-correlate with accretion rates (Wang et al. 2004). For the SEAMBH2012 sample, we monitored nine NLS1s successfully, whose names and coordinates are summarized in Table 1 of Paper II.

Table 1
Stellar Template

Object	Stellar Template	Spectral Type[a]
Mrk 335	HD 77818	K1 IV
Mrk 1044	HD 173399	G5 IV
IRAS 04416+1215	HD 10307	G1.5 V
Mrk 382	SAO 126242	F7 Vw
Mrk 142	HD 142373	F8 Ve...
MCG +06-26-012	HD 131156	G8 V
IRAS F12397+3333	HD 118100	K5 Ve
Mrk 486	HD 20618	G6 IV
Mrk 493	HD 118100	K5 Ve

Note. — Name and spectral type of the selected template for the comparison stars.

[a] The spectra type listed in Valdes et al. (2004).

2.2. *Spectroscopy and Data Reduction*

All of the spectroscopic observations were carried out with the Yunnan Faint Object Spectrograph and Camera which is mounted on the Lijiang 2.4-m telescope at the Yunnan Observatories of the Chinese Academy of Sciences. To obtain spectra with highly accurate flux calibration, we oriented the long slit to take the spectra of the object and a nearby non-varying comparison star (used as standard) simultaneously. This method was applied to RM campaign early in Maoz et al. (1990) and Kaspi et al. (2000). In SEAMBH2012, we fixed the slit width to 2″.5 given the seeing conditions, and used Grism 14 with a resolution of 92 Å mm^{-1} and a wavelength coverage of 3800-7200Å which yields $\sim 1.8\,$pixel^{-1} ($\sim$ 108 km s^{-1} pixel^{-1}) in dispersion direction finally. All of the spectroscopic data were reduced with IRAF v2.16 and the flux was calibrated by comparing spectra of the targets with those of the comparison stars exposured in the slit. Readers are referred to Paper I for more details.

3. CORRECTION FOR LINE-BROADENING

In spectroscopic observation, the line-broadening (ξ), which is caused by seeing and instruments (e.g., grism or grating), influences the observed profiles of emission lines. Although the instrumental settings remain the same during observations, the seeing varies nights by nights (FWHM of the point-spread functions in SEAMBH2012 is generally from 1″.2 to 2″.5, while the width of slit is fixed to 2″.5 which is wider than seeing), and ξ in each night changes as well. Furthermore, the mis-centering of objects and comparison stars in the slit is not a constant in different nights. This causes that each spectrum have slightly different shift in dispersion direction. Fortunately, we are also able to estimate the shifts from the spectra of comparison stars so that we can correct this automatically by deconvolution.

The observed Hβ profile of $I_{\rm obs}$ is a convolution of its in-

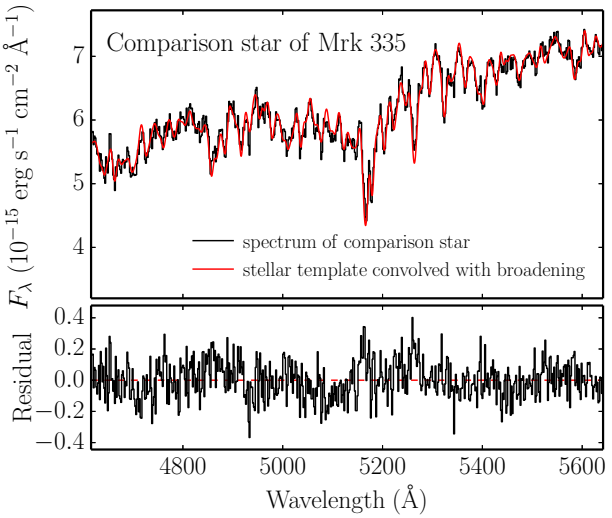

Figure 2. An individual-night spectrum of the comparison star of Mrk 335 and its best fitting model. The top panel shows the observed spectrum (black line) of the star and the best model (red line). The bottom panel is the residual.

trinsic profile $I_{\rm int}$ and the line-broadening function ξ, namely

$$I_{\rm obs}(\lambda) = I_{\rm int}(\lambda) \otimes \xi(\lambda) = \int I_{\rm int}(\lambda')\xi(\lambda-\lambda')d\lambda'. \qquad (1)$$

Variations of ξ does not change the integrated flux of Hβ emission line, however, it blurs $I_{\rm int}$ and further influences the velocity-resolved time series analysis. It is thus expected to correct the line-broadening of Hβ profiles before the velocity-resolved RM analysis, especially for those objects with relatively narrow Hβ lines (FWHM $\sim$ 1000 – 2000km/s, comparing to the instrumental broadening of $\sim$500km/s estimated in Paper I) in our SEAMBH2012 observation. Fortunately, the spectra of comparison stars in the same slit during spectroscopic exposures can be employed to estimate ξ accurately in light of that the FWHM of absorption lines in stellar spectra ($\lesssim 10{\rm km\,s^{-1}}$) is much narrower than the line-broadening. An efficient way to perform such a correction is the well-known Richardson-Lucy algorithm (Richardson 1972; Lucy 1974) which can deconvolve ξ from $I_{\rm obs}$ so as to recover $I_{\rm int}$.

Figure 1 shows the sketch of procedures for line-broadening correction. We first estimate the broadening function ξ of exposure via fitting the spectrum of comparison star in each night by a stellar template, then use the obtained ξ to correct the broadening of Hβ profile $I_{\rm obs}$ in the observed spectra through Richardson-Lucy deconvolution algorithm. Finally, we can get the broadeing-corrected profile $I_{\rm int}$.

3.1. *Richardson-Lucy Deconvolution*

Richardson-Lucy (R-L) deconvolution algorithm is a Bayesian-based iterative technique commonly used for recovering signal blurred by a known response. It has been widely adopted to improve the spatial resolution of images from Hubble Space Telescope (*HST*, e.g., Lauer et al. 1993; Snyder et al. 1993; Lauer et al. 1995; Gebhardt et al. 1996; Schmitt & Kinney 1996; Kormendy & Bender 1999; Farrah et al. 2001; Rest et al. 2001; Lauer et al. 2005 and the references therein), and to correct the instrumental broadening in spectroscopic data such as ultraviolet spectra from Goddard High Resolution Spectrograph on *HST* (e.g., Wahlgren et al. 1991; Brandt et al. 1993; Bomans et al. 1996) or X-ray spectroscopy measurements of heavy elements

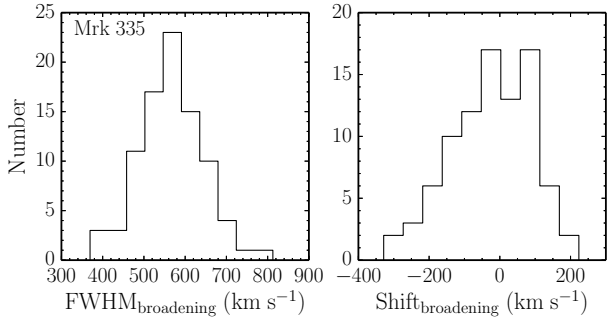

Figure 3. The distribution of the broadening functions ξ of Mrk 335 obtained by fitting the stellar spectra. The left panel shows the distribution of FWHM of ξ in each night, and the right panel shows the distribution of their shifts.

(Fister et al. 2007). Even recently, Menezes et al. (2014) used it in data analysis of integral field spectrograph from Gemini. To our knowledge, this is the first application of such technique to the correction of instrumental broadening in spectra from RM observation.

We do not repeat the details of R-L deconvolution here, but just give a brief description (readers may refer to original papers Richardson (1972) and Lucy (1974)). In short, if $I^n_{\rm int}$ is the n-th estimate of the intrinsic profile in the iterative sequence, the $(n+1)$-th estimate is obtained by

$$I^{n+1}_{\rm int}(\lambda') = I^n_{\rm int}(\lambda') \int \frac{I_{\rm obs}(\lambda)}{I^n_{\rm obs}(\lambda)}\xi(\lambda-\lambda')d\lambda, \qquad (2)$$

where

$$I^n_{\rm obs}(\lambda) = \int I^n_{\rm int}(\lambda')\xi(\lambda-\lambda')d\lambda'. \qquad (3)$$

Similar to the widely used equidistribution of ignorance in Bayes's postulate, we assume a uniform distribution as the initial guess of intrinsic profile, so that $I^0_{\rm int}(\lambda) = \int I_{\rm obs}(\lambda)d\lambda \,/\, \int d\lambda$. After a certain number (see Section 3.3) iterations, the intrinsic profile can be recovered effectively.

3.2. *Line-broadening Function*

During the spectroscopic exposures, we oriented the slit in order to simultaneously include the target and a nearby comparison star for their spectra (an object-star pair). It enables us to obtain ξ of the object synchronously from the comparison star in the pair. To estimate the broadening function, we use the direct pixel-fitting method similar to Greene & Ho (2006) and Ho et al. (2009). The observed spectrum $\mathcal{S}$ of comparison star is modeled by a stellar template spectrum $\mathcal{T}$ convolved by the broadening function:

$$\mathcal{S}(\lambda) = \mathcal{P}(\lambda)[\mathcal{T}(\lambda) \otimes \xi(\lambda)]. \qquad (4)$$

Here, $\mathcal{P}$ is a polynomial accounted for large-scale mismatch in the continuum shape of the comparison star and template. In this work, we assume ξ a Gaussian function and select the most similar stellar spectrum as the template of comparison star from the Indo-U.S. Library of Coudé Feed Stellar Spectra[10] (Valdes et al. 2004). The selected templates for the comparison stars are listed in Table 1. In order to get the line-broadening function close enough to Hβ, we set the fitting window to 4500Å-5500Å in rest frame of the objects. Prior to the fitting, the consecutive exposures of the object-star pair in each night are combined so as to provide high S/N ratio. The

[10] http://www.noao.edu/cflib/

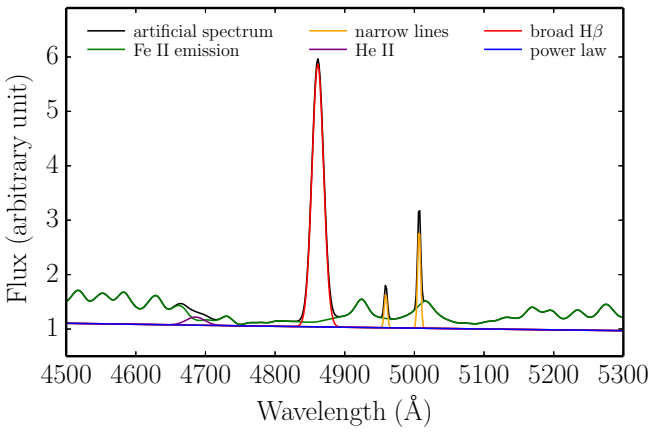

Figure 4. Artificial AGN spectrum in the Monte Carlo simulation. The black line is the created artificial AGN spectrum. The components are: (a) a power-law continuum (blue); (b) Fe II emission (green) and broad He II (purple); (c) narrow emission lines of [O III]$\lambda\lambda$4959,5007 (orange) and (d) a broad component of Hβ (red).

best values of FWHM and shift in ξ are determined by fitting the combined spectrum of the comparison star in each night via Levenberg-Marquardt algorithm.

An example of individual-night spectrum of the comparison star and the best model for Mrk 335 is shown in Figure 2. The distributions of FWHM and shift of ξ during the observation of Mrk 335 are shown in Figure 3. The FWHM, on average, is consistent with the mean value of 500km s^{-1} estimated in Paper I. However, through the fitting here, we are able to measure the broadening function in each individual night. For the other objects, the distributions of the broadening are similar to the case of Mrk 335, so we do not show them repeatedly here. It should be noted that, although SEAMBHs generally have weak [O III]λ5007, we can still try to estimate ξ from the [O III] line in several objects with relatively strong and intrinsicly narrow [O III] (e.g., Mrk 382) by comparing its width to the value of spectra with higher resolution (Whittle 1992), if we assume the narrow lines do not vary with time. The ξ obtained from [O III] is consistent with the values estimated by the fitting here, and the differences are $\lesssim$ 50km s^{-1} averagely.

After getting ξ in each night (for each target), we reconstruct $I_{\rm int}$ by applying R-L deconvolution to the observed spectra $I_{\rm obs}$ of the objects.

3.3. *Iteration Number*

The termination of iterations is one of the core issues in R-L deconvolution. Too few iterations are insufficient for reconstruction of the original signal, while an excess of iterations magnifies high-frequency noise and even produces nonsense results (Lucy 1974). Here, a simple Monte Carlo approach is used to determine the appropriate number for terminating the iterations.

For each object, we first construct an Gaussian, with the same FWHM and equivalent width (EW) of Hβ in the observed mean spectra, where the mean broadening of 500 km s^{-1} estimated in Paper I have been subtracted, as the artificial intrinsic spectrum. This artificial intrinsic spectrum is used to generate a mock observed spectrum $I_{\rm obs}$ in each individual night by convolving with ξ obtained from the fitting in Section 3.2 and adding random noises with the same level of S/N as the truly observed spectrum. Then, we select the iteration number which can get the best reconstruction (with the smallest χ^2) of the artificial intrinsic spectrum by de-convolving ξ

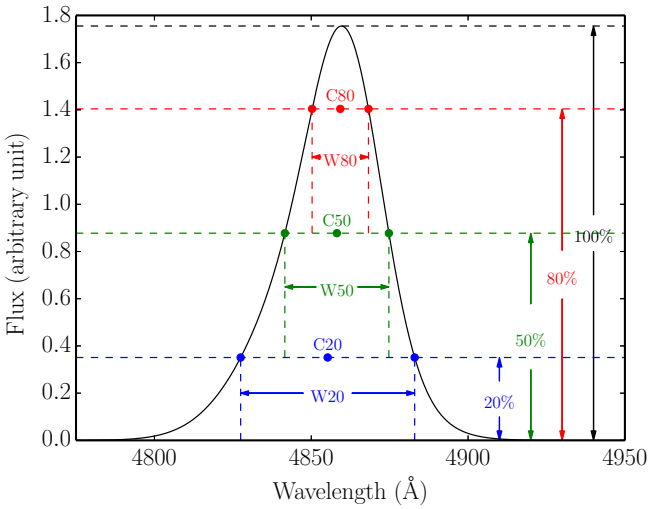

Figure 5. Definition of (W20, W50, W80) and (C20, C50, C80). These parameters can be used as indicators to characterize the profile of emission line.

from the mock $I_{\rm obs}$ as the optimal number of iterations. The mock $I_{\rm obs}$ is generated 20 times for each spectrum, and the median value of the optimal numbers of iterations obtained by the above procedure is chosen as the final iteration number of the deconvolution.

3.4. *Host Galaxy Subtraction*

The spectra of AGNs and comparison stars are smeared by the same broadening function every night since both of them are point sources. However, the host galaxies of the objects are extended and their spectra are affected by broadening which is different from those of comparison stars. Therefore, before de-convolving the spectra of AGNs with the broadening function obtained from the comparison stars in Section 3.2, the contribution of host galaxies should be removed. Paper III has already decomposed the spectra and extracted the contribution of host galaxies by fitting scheme. We simply subtract those host contributions, which we got in Paper III, from the spectra of objects before the procedures of deconvolution to avoid potential influence of different broadening in host galaxies.

3.5. *Monte Carlo Simulation on Deconvolution*

We make use of Monte Carlo simulation to evaluate the robustness of reconstructing the intrinsic profile of Hβ line through the R-L deconvolution. We first create an artificial AGN spectrum by including (a) a power-law continuum; (b) Fe II emission and broad He II; (c) narrow emission lines of Hβ and [O III]$\lambda\lambda$4959,5007 and (d) a broad component of Hβ. The components here are almost the same as the model we used in Paper III except for the absence of host galaxy contribution (host does not influence the profiles of Hβ in the simulation). We set the FWHM and EW of Hβ in the artificial AGN spectrum to 1200km/s and 100Å (see Figure 4), respectively, which are the typical values in the present sample. In order to test the precision of recovery by the deconvolution in the cases with various broadening and S/N ratio, we broaden the artificial spectrum by different broadening function and plus stochastic noise to generate the simulated observed spectra. In the meantime, we select a stellar spectral template (HD 44951 used here) from the Indo-U.S. Library and broaden it with the same broadening as the AGN spectrum and plus noise

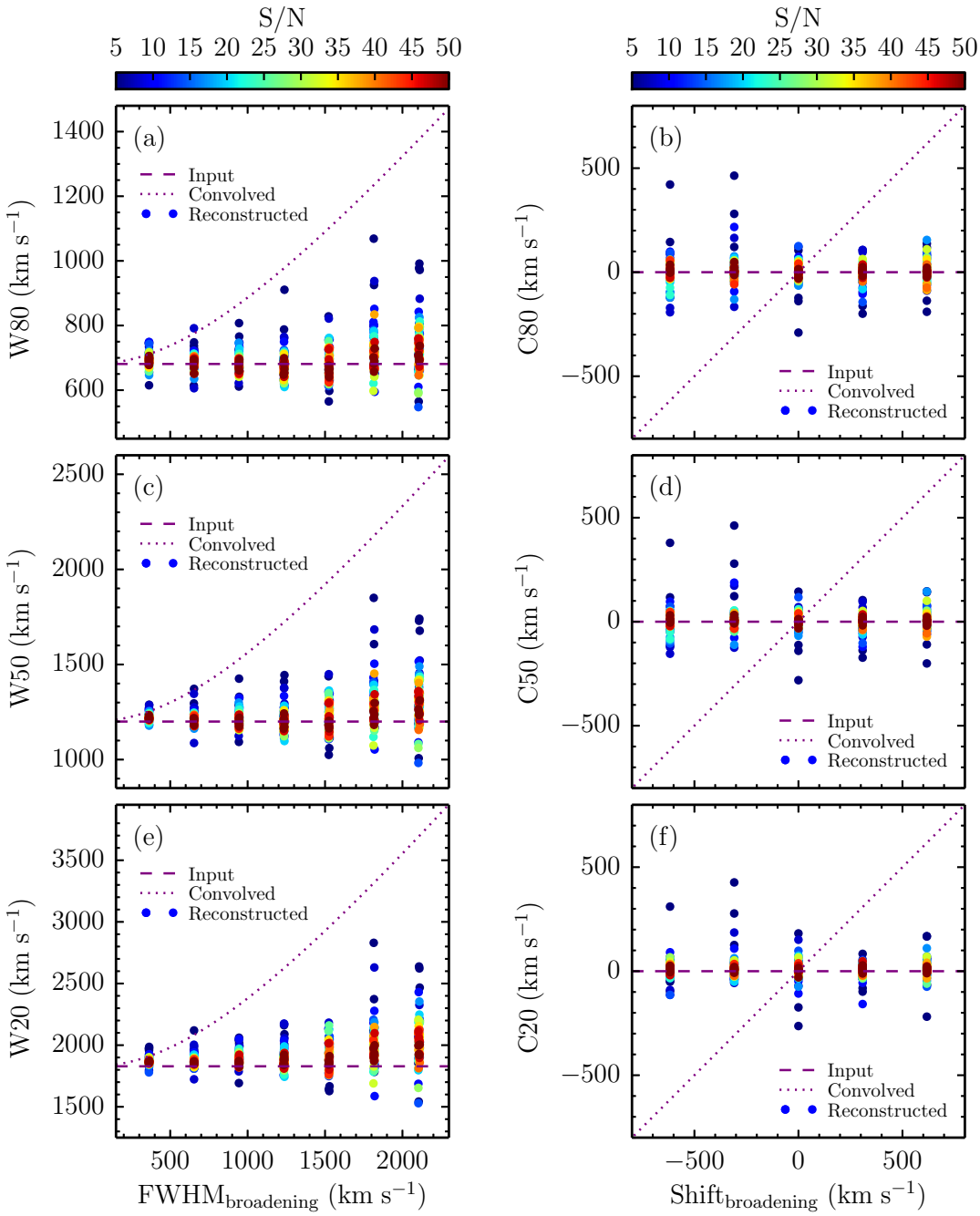

Figure 6. Comparisons of Hβ profiles between the input and output spectra in the Monte Carlo simulation. FWHM$_{\rm broadening}$ and Shift$_{\rm broadening}$ are the width and shift of broadening function ξ . The dashed lines mark the values of (W20, W50, W80) and (C20, C50, C80) in the input artificial spectrum, while the dotted lines show their values in the convolved output spectra. The points are (W20, W50, W80) and (C20, C50, C80) of the profiles in the reconstructed spectra after the deconvolution. The colors show the S/N ratios we set in the simulated observed spectra. The reconstruction is more successful in the cases of narrower broadening function and higher S/N ratios.

as well. We take the simulated observed AGN and star spectra as the input of the procedures in Section 3, and then compare the profiles of Hβ in the output reconstructed spectra to those of the original artificial AGN spectra.

To elaborate the comparison of profiles between the spectra before and after the deconvolution procedures, we define full width at (20%, 50%, 80%) of maximum as (W20, W50, W80), and centers at (20%, 50%, 80%) of maximum as (C20, C50, C80) to characterize the profiles of Hβ (please see Figure 5 for their definition). (W20, W50, W80) evaluate the width of emission line at different height, while (C20, C50, C80) show the shifts at the corresponding levels (see figure 5). Here, W50 is just simply FWHM in the common sense. The comparison of emission-line profiles before and after the deconvolution in the Monte Carlo simulations is shown in Figure 6. Generally speaking, the deconvolution can recover the profile of Hβ correctly. (W20, W50, W80) and (C20, C50, C80) of the reconstructed Hβ profiles are consistent with the value of the input artificial AGN spectrum in the cases with high S/N ratios. The reconstruction is more successful in the

cases with narrower broadening function and higher S/N ratio, especially when the FWHM of broadening is narrower than the input Hβ profile. The widths of Hβ in the observed spectra of SEAMBH2012 are 1000 $\sim$ 2000 km s^{-1}, while the broadening is only $\sim$ 500 km s^{-1}. And the S/N ratio of spectra in SEAMBH2012 is generally higher than 20. Therefore, the intrinsic profiles recovered by the deconvolution Section 3 is reliable.

3.6. *Profiles Before and After the Deconvolution*

In order to give an overall evaluation how effectively does the deconvolution work, examples of the comparison between observed and de-convolved spectra of Mrk 335 are provided in Figure 7. It is very obvious that the deconvolution procedures correct the broadening and mis-centering effect successfully. To further compare the profiles before and after the deconvolution, we measure (W20, W50, W80) and (C20, C50, C80) of Hβ in the spectra before and after the deconvolution procedures. As an example, the values of Mrk 335 are shown in Figure 8. After the deconvolution, the widths (W20, W50, W80) of its Hβ lines narrow down for $\sim$(6%, 15%, 20%) on average. In particular, the distribution of W80 in the reconstructed spectra becomes much narrower, which means the more serious influence caused by the broadening around the peak (the highest and narrowest part) of emission line, than in its wing part (with broader width), have been corrected effectively. Additionally, the centers at different levels (C20, C50, C80) are more concentrated than the cases before the deconvolution. The comparison before and after the deconvolution demonstrates the validity of the deconvolving procedures used in the present paper. The centers, it should be noted, do not locate on 0 km s^{-1} because the zero here is defined by the redshift queried from NASA/IPAC Extragalactic Database[11].

4. VELOCITY-RESOLVED TIME SERIES ANALYSIS

4.1. *Methods*

The light curves and the time delays between the variations of the continuum at 5100Å and Hβ fluxes measured by simply integrating the full extent of the emission lines have been published in Paper I and II. Paper III updated these measurements by introducing a sophisticated scheme that fit AGN continuum, host contribution in the slit and emission lines simultaneously. The updated time lags are consistent with the previous ones but have smaller uncertainties (see the comparison in Paper III). However, these time delays only stand for the radii averaged by the emissivity function of BLRs, and no information of velocity fields is carried out. In this section, we focus on the velocity-resolved analysis of delays in order to reveal the kinematics of BLR clouds in SEAMBHs.

The procedures of deconvolution in Section 3 have removed the varying line-broadening from the observed profiles and almost corrected the wavelength shifts caused by mis-centering. After further correcting the remanent shifts ($\lesssim$ 50 km s^{-1}) using [O III]λ5007 line as our wavelength reference, the spectra are ready for velocity-resolved time series analysis. RMS (root of mean-square) spectra of the objects are obtained in the standard way from the spectra after the line-broadening correction. Similar to many previous works (e.g., Bentz et al. 2008, 2009b; Denney et al. 2009a,b; Bentz et al. 2010; Denney et al. 2010; Grier et al. 2013), we divide Hβ emission line into several bins in velocity space, where each bin has equal amount of flux in the RMS spectrum. After integrating the flux of emission line in each bin, we cross-correlate the obtained individual-bin light curves to the continuum light curve at 5100Å. Due to the lack of error bars in the output spectra of deconvolution, we estimate the uncertainties of flux in the individual-bin light curves based on the differences between adjacent points using median filter as in Paper I. The interpolation cross-correlation function (ICCF; Gaskell & Sparke 1986; Gaskell & Peterson 1987; White & Peterson 1994) is employed, and the centroid of the CCF, above 80% of the maximum cross-correlation coefficient ($r_{\rm max}$), is adopted as the time lags (e.g., Koratkar & Gaskell 1991; Peterson et al. 2004; Denney et a. 2006; Bentz et al. 2009b; Denney et al. 2010 and reference therein). The uncertainties in the measured lag time are determined through the Monte Carlo "flux randomization/random subset sampling" method described in Maoz & Netzer (1989) and Peterson et al. (1998, 2004). The rest-frame velocity-resolved time lags of the objects, as well as their RMS spectra created after deconvolution, are shown in Figure 9 and 10. The details of objects are discussed below.

[11] http://ned.ipac.caltech.edu/

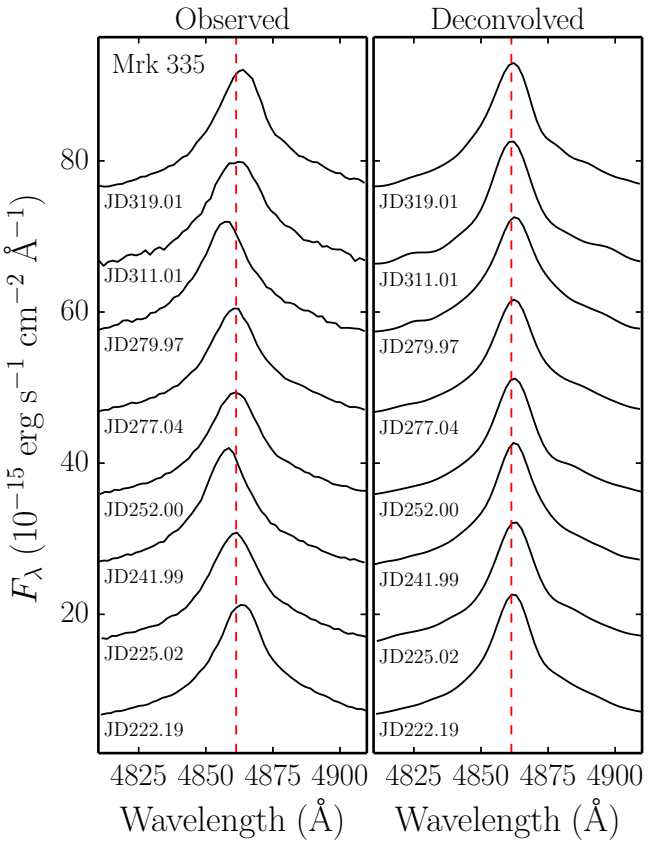

Figure 7. A comparison of deconvolved profiles (Mrk 335) with the observed ones. The profiles are shifted vertically by a constant value (10^{-14} erg s^{-1} cm^{-2-1}) from bottom to top for recognition. The broadening caused by instruments and varying seeing is corrected successfully. The mis-centering effect (see Section 3) is also eliminated effectively. The dashed lines mark the center of H$\beta\lambda$4861. The wavelength is in the rest-frame and JD-2456000 is marked next to each profile.

4.2. *Individual Objects*

Mrk 335. The Hβ emission line of this object is divided into eight bins in velocity space, where each bin contains 1/8 of the variable line flux in its RMS spectrum. Its

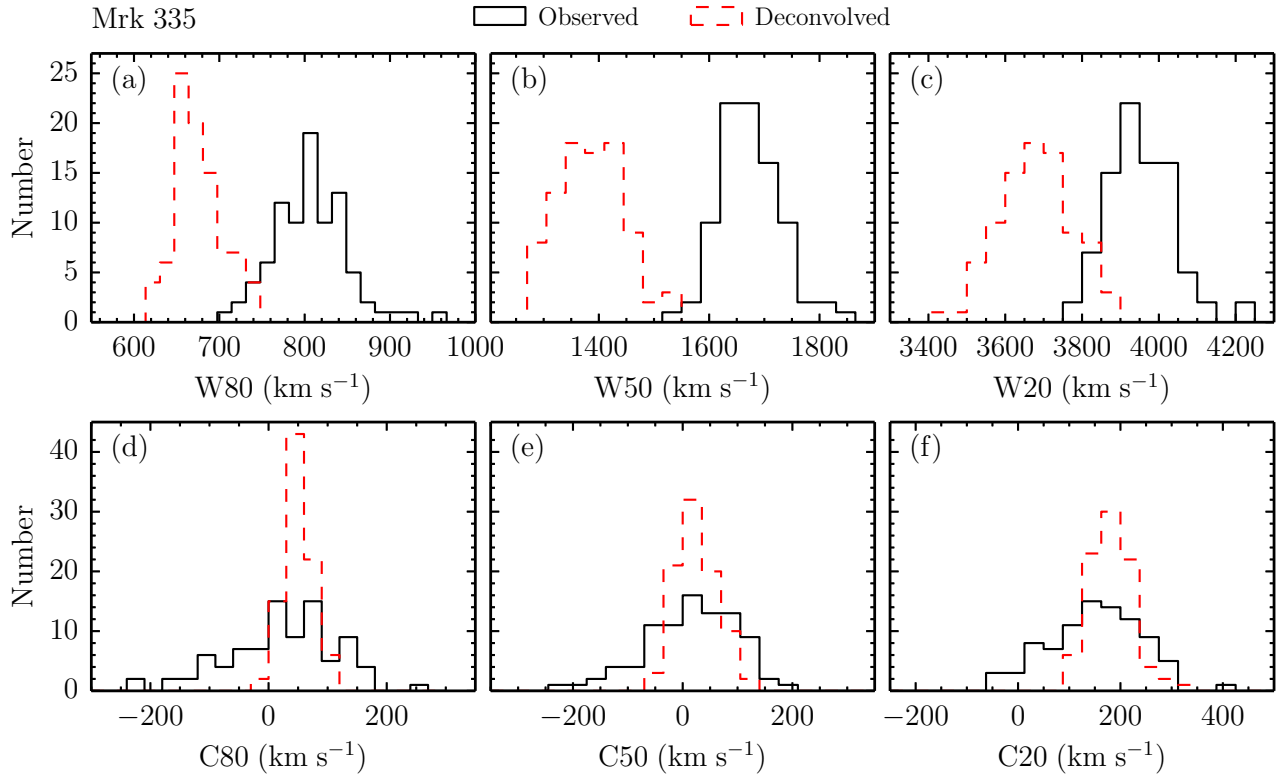

Figure 8. A comparison of widths and shifts before and after the deconvolution (Mrk 335). Panels (a) - (f) are W80, W50, W20, C80, C50 and C20, respectively. The black solid lines are the distributions in the observed profiles, and the red dashed lines are the distributions in the reconstructed profiles after the deconvolution.

velocity-resolved time series analysis (see Figure 9) demonstrates clear gradient in the delays of different velocity bins that the blueshifted part of Hβ lags the response in its redshifted part (from $\sim$ 25 days in the blue end to $\sim$ 5 days in the red end). This kinematic signature is consistent with the expectation of inflow that the gas on near side is receding to the observer while the gas on opposite side is approaching. In Figure 9, we also show the result before the deconvolution. Generally speaking, the velocity-resolved time delays before and after the deconvolution are consistent with each other. However, the deconvolution-corrected result show some details, more clearly, that the longer time delays in blueshifted part vary gently while the lags in the redshifted part decrease more quickly. The before-deconvolution time lags only show uniform gradient from blue- to red-shifted velocity. In particular, the RMS spectrum before the deconvolution contains relatively stronger contribution of narrow Hβ emission line which is caused by the varying width of narrow line (because of the changing broadening in each night), while this feature is much weaker in the RMS spectrum of the reconstructed profiles. The comparison in Figure 9 also indicates that the deconvolution procedures can recover the velocity-resolved information moderately in RM time-series analysis.

Before our observation, Mrk 335 was monitored twice in 1989–1996 (Kassebaum et al. 1997; Peterson et al. 1998) and 2010–2011 (Grier et al. 2012), respectively. Its velocity-resoved time lags in the latter campaign have been published in Grier et al. (2013). It is not unexpected that the inflow signature in the velocity-resoved delays presented here is consistent with the previous measurements in 2010–2011 (Grier et al. 2013), given the short time interval between these two campaigns. Such a kind of signature has also been reported in the velocity-resolved delay analysis of many other sources like Arp 151 (Bentz et al. 2008, 2009b), NGC 3516 (Denney et al. 2009a, 2010), Mrk 1501 (Grier et al. 2013) and PG 2130+099 (Grier et al. 2013).

Mrk 142. The velocity-resolved time delays of Mrk 142 are reported here for the first time. It was previously monitored by the LAMP collaboration (Bentz et al. 2009b), however the authors do not show its velocity-resolved lags perhaps due to their data quality. The observation in our campaign has more homogeneous cadence and better calibration precision. Opposite to the case of Mrk 335, Mrk 142 shows signature of outflow indicated by the shorter time lag from BLR gas in the blueshifted side of Hβ line comparing with the gas in redshifted side. Interestingly, to our knowledge, the signature of outflow was observed distinctly by reverberation mapping in only one case, NGC 3227 (Denney et al. 2009a, 2010), before the detection shown here. Comparing with the low accretion rate in NGC 3227 (Denney et al. 2010; Paper IV), Mrk 142 is a SEAMBH and radiation pressure acting on the ionized gas is probably the driver for the observed outflow.

Mrk 486. It also demonstrates clear signature of infalling gas as the case of Mrk 335. Except for the first bin, the response to the continuum variation in the blueshifted gas lags the response of the gas corresponding to the redshifted side.

Mrk 1044. The velocity-resolved lags of Mrk 1044 are relatively symmetric and show evidence of simple virialized motions, that high-velocity gas is located in the more central region, which is similar to the cases of NGC 5548 (Denney et al. 2009a), SBS 1116+583A (Bentz et al. 2009b), Mrk 1310 (Bentz et al. 2009b), NGC 4051 (Denney et al. 2009b, 2010) and 3C 120 (Grier et al. 2013) in the previous works.

MCG +06-26-012. A signature of outflow is shown in this

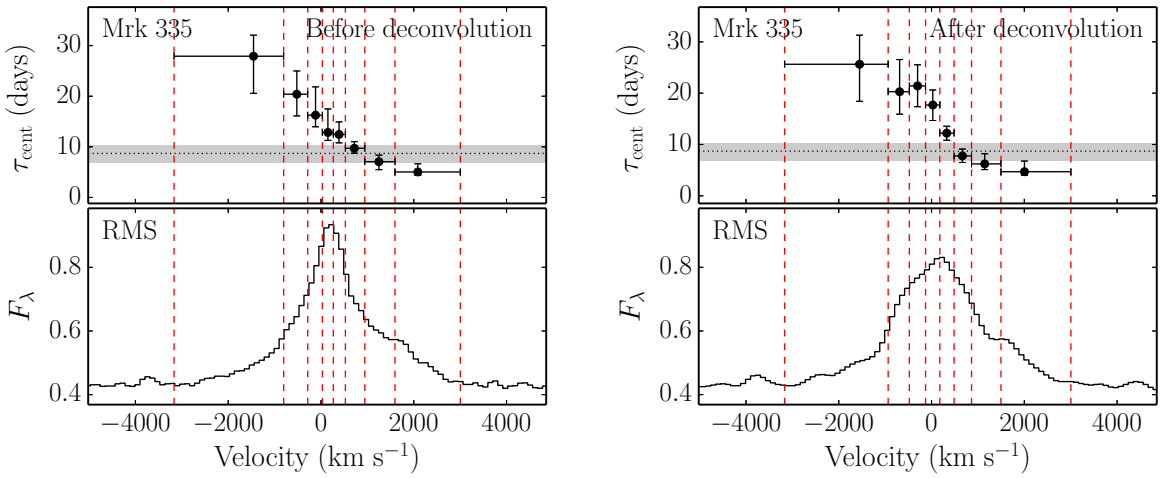

Figure 9. Rest-frame velocity-resolved time delays and the corresponding RMS spectra. The result of Mrk 335 obtained from the spectra without deconvolution is shown in the left plot, and its result from deconvolved spectra is shown in the right one. The upper panel of each plot shows the centroid time lags in the divided velocity bins, and the lower panel is their RMS spectrum (in units of 10^{-15} erg s^{-1} cm^{-2} $^{-1}$). The red dashed lines are edges of the bins. The horizontal dotted line and the gray band mark the average time lag and the uncertainties provided in Paper III. The horizontal error bar in upper panel denote the velocity bin, while the vertical error bar is the uncertainty of the lag.

object that the time delays ($\sim$ 20 days) in the blue part of Hβ are slightly shorter than those ($\sim$ 30 days) in the red part, however, the outflow signs are ambiguous a little bit because of the large errors. The large error bars are caused by the inhomogeneous sampling and the short monitoring period comparing with the variation in the light curves. MCG +06-26-012 is the only sub-Eddington object in the present sample (see details in Paper II).

Mrk 382. The lags in different velocity bins are undistinguished. This phenomenon has been found in other objects, such as Mrk 1310 (Bentz et al. 2009b), NGC5548 (Bentz et al. 2009b) and Mrk 290 (Denney et al. 2010). This may be either caused by that the lag differences among the bins are smaller than their error bars (by the quality of the current data), or it could be real intrinsically that those bins have the same time lags. If the line-of-sight velocity keeps a constant in the BLR, motion of cloud are fully chaotic. This remains open for future observations with high quality data.

IRAS F12397+3333 and **Mrk 493** are similar to Mrk 382.

IRAS 04416+1215. The direct integrating method in Paper I and II is failed to give the average time lag of its integrated Hβ emission line flux. Only multi-components fitting method in Paper III is able to detect its delay. Here, we adopt the direct integrating method to measure the light curves after the division of bins and still fail to get reliable detection of its velocity-resolved lags. We divide its Hβ into two bins and demonstrate the result here for completeness. The $r_{\rm max}$ in the redshifted bin is only $\sim$ 0.4.

5. DISCUSSIONS

Outflows suggested by the observation of blueshifted broad absorption lines are not rare in AGNs (e.g., Trump et al. 2006; Gibson et al. 2009 and reference therein). However, how do the outflows contribute to broad emission lines, especially in high accretion rate AGNs, is still subject to some debate. Considering that super-Eddington accreting AGNs probably have the strongest radiation pressure, which can provide kinetic energy to BLR gas, among the whole AGN populations, the possibilities of outflows that occur in SEAMBHs maybe doubt to be higher than sources with normal accretion rates. However, the present sample, although with its limited size, shows diverse properties of the BLR kinematics, rather than the simple outflows (there is only one from the detected four SEAMBHs, except for MCG +06-26-012 with low accretion rate). It is consistent with the fact that the observed profile of Hβ in the present sample does not show unified signature of blueshifted asymmetry. On the other hand, there are a few objects (2 out of 4 super-Eddington AGNs) showing clear evidence for the presence of infalling gas in BLRs. Considering the fact that objects in the present sample are super-Eddington accreting AGNs, the velocity fields of the surrounding gas showing infall in kinematics are not surprising. Otherwise, a significant fraction of the accreting gas will be channelled into outflows, making fast growth of less massive black holes be suppressed. It is impossible to reach a conclusion about the pattern of velocity fields of ionised gas in the vicinity of black holes in super-Eddington accreting AGNs. We hope increases of monitored SEAMBHs and normal AGNs could clarify the patterns of the velocity fields.

6. CONCLUSIONS

We have presented here velocity-resolved time lag measurements of nine objects observed in our SEAMBH2012 campaign. To correct the line-broadening caused by instruments and seeing, we use Richardson-Lucy deconvolution to reconstruct Hβ profiles. The broadening function in each night is estimated by fitting the spectra of the stars observed simultaneously with stellar templates, and Monte Carlo method is adopted to test the validity of the broadening-correction procedures. We show that the Richdson-Lucy iteration is an efficient method to recover the velocity-resolved information to some extent.

All of the objects in the present sample are NLS1s with very high accretion rates except for MCG +06-26-012. Five sources among them demonstrate clear velocity-resolved time delays in their Hβ emission lines. The velocity-resolved lags of Mrk 335 and Mrk 486 show the signature of gas infall, while the BLR clouds in Mrk 142 and MCG +06-26-012 tend to be radial outflowing. The symmetric pattern of Mrk 1044 is consistent with virialized motions. The time lags of the other four objects are not velocity-resolvable. We do not find significant differences in the BLR kinematics of SEAMBHs,

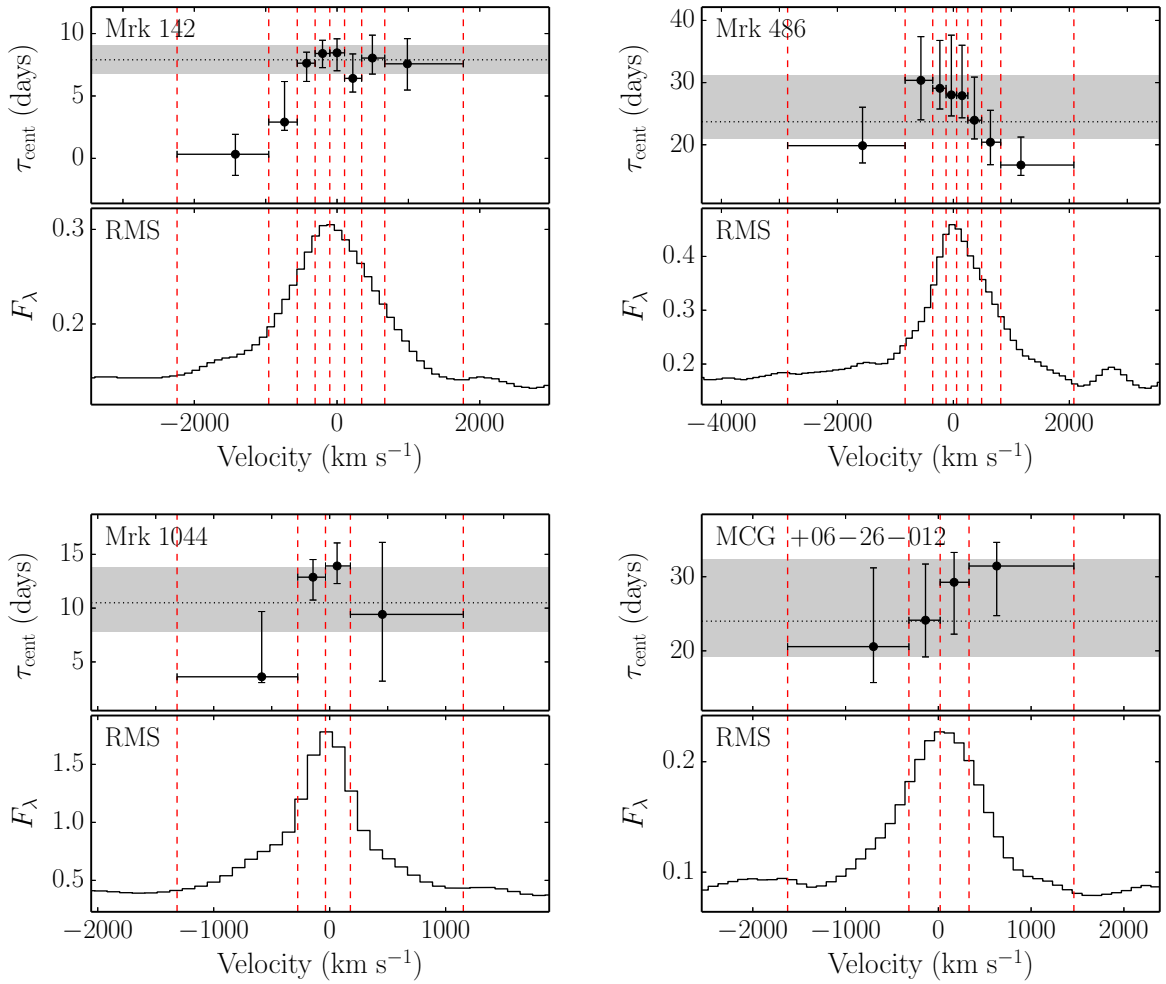

Figure 10. Rest-frame velocity-resolved time delays and the corresponding RMS spectra. The meanings of panels, symbols, lines and units are the same as in Figure 9.

comparing with sub-Eddington AGNs. Some discussions for the result of each individual object are provided in the main text. This analysis provides new insight into the geometry and kinematics of BLRs in SEAMBHs.

We acknowledge the support of the staff of the Lijiang 2.4m telescope. Funding for the telescope has been provided by CAS and the People's Government of Yunnan Province. This research is supported by the Strategic Priority Research Program - The Emergence of Cosmological Structures of the Chinese Academy of Sciences, Grant No. XDB09000000, by NSFC grants NSFC-11173023, -11133006, -11373024, -11233003, -11503026, -11573026 and -11473002, a NSFC-CAS joint key grant U1431228, the China-Israel nsfc-isf 11361140347 and by the Key Research Program of the Chinese Academy of Sciences, Grant No. KJZD-EW-M06.

REFERENCES

Bahcall, J. N., Kozlovsky, B.-Z., & Salpeter, E. E. 1972, ApJ, 171, 467
Barth, A. J., Bennert, V. N., Canalizo, G., et al. 2015, ApJS, 217, 26
Barth, A. J., Pancoast, A., Bennert, V. N., et al. 2013, ApJ, 769, 128
Barth. A. J., Pancoast, A., Thorman, S. J., et al. 2011, ApJ, 743, 4
Bentz, M. C., Denney, K. D., Grier, C. J., et al. 2013, ApJ, 767, 149
Bentz, M. C., Walsh, J. L., Barth, A. J., et al. 2008, ApJ, 689, L21
Bentz, M. C., Walsh, J. L., Barth, A. J., et al. 2009, ApJ, 705, 199
Bentz, M. C., Walsh, J. L., Barth, A. J., et al. 2010, ApJ, 716, 993
Blandford, R. D., & McKee, C. F. 1982, ApJ, 255, 419
Boller, T., Brandt, W. N., & Fink, H. 1996, A&A, 305, 53
Bomans, D. J., de Boer, K. S., Koornneef, J., & Grebel, E. K. 1996, A&A, 313, 101
Boroson, T. A., & Green, R. F. 1992, ApJS, 80, 109
Brandt, J. C., Heap, S. R., Beaver, E. A., et al. 1993, AJ, 105, 831
Denney, K. D., Bentz, M. C., Peterson, B. M., et al. 2006, ApJ, 653, 152
Denney, K. D., Peterson, B. M., Pogge, R. W., et al. 2009a, ApJ, 704, L80
Denney, K. D., Peterson, B. M., Pogge, R. W., et al. 2010, ApJ, 721, 715
Denney, K. D., Watson, L. C., Peterson, B. M., et al. 2009b, ApJ, 702, 1353
Du, P., Hu, C., Lu, K.-X., et al. (SEAMBH Collaboration) 2014, ApJ, 782, 45 (Paper I)
Du, P., Hu, C., Lu, K.-X., et al. (SEAMBH Collaboration) 2015, ApJ, 806, 22 (Paper IV)
Farrah, D., Rowan-Robinson, M., Oliver, S., et al. 2001, MNRAS, 326, 1333
Fister, T. T., Seidler, G. T., Rehr, J. J., et al. 2007, Phys. Rev. B, 75, 174106
Gaskell, C. M. 2009, NewAR, 53, 140
Gaskell, C. M., & Peterson, B. M. 1987, ApJS, 65, 1
Gaskell, C. M., & Sparke, L. S. 1986, ApJ, 305, 175
Gebhardt, K., Lauer, T. R., Byun, Y.-I., et al, 1996, AJ, 112, 105
Gibson, R. R., Jiang, L., Brandt, W. N., et al. 2009, ApJ, 692, 758
Greene, J. E., & Ho, L. C. 2006, ApJ, 641, 117
Grier, C. J., Peterson, B. M., Horne, K., et al. 2013, ApJ, 764, 47
Grier, C. J., Peterson, B. M., Pogge, R. W., et al. 2012, ApJ, 755, 60
Ho, L. C. 2004, ARA&A,
Ho, L. C., Greene, J. E., Filippenko, A. V., & Sargent, W. L. W. 2009, ApJS, 183, 1

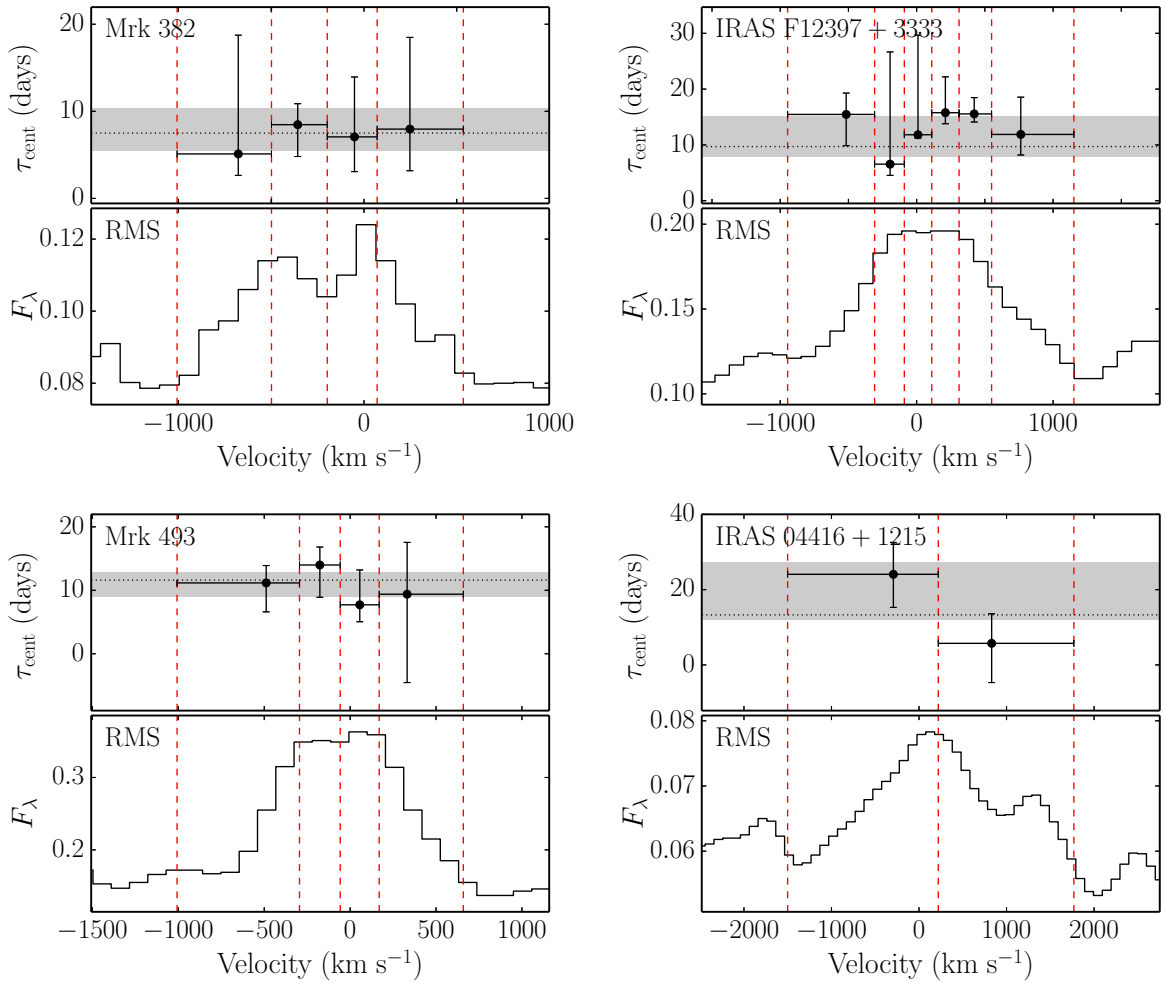

Figure 10. Continued.

Horne, K. 1994, in ASP Conf. Ser. 69, Reverberation Mapping of the Broad-Line Region in Active Galactic Nuclei, ed. P. M. Gondhalekar, K. Horne, & B. M. Peterson (San Francisco: ASP), 23
Horne, K., Peterson, B. M., Collier, S. J., & Netzer, H. 2004, PASP, 116, 465
Hu, C., Du, P., Lu, K.-X., et al. (SEAMBH Collaboration) 2015, ApJ, 804, 138 (Paper III)
Kaspi, S., Brandt, W. N., Maoz, D., et al. 2007, ApJ, 659, 997
Kaspi, S., Smith, P. S., Netzer, H., et al. 2000, ApJ, 533, 631
Kassebarm, T. M., Peterson, B. M., Wanders, I., et al. 1997, ApJ, 475, 106
Koratkar, A. P., & Gaskell, C. M. 1991, ApJS, 75, 719
Kormendy, J., & Bender, R. 1999, ApJ, 522, 772
Lauer, T. R., Faber, S. M., Groth, E. J., et al. 1993, AJ, 106, 1436
Lauer, T. R., Ajhar, E. A., Byun, Y.-I., et al. 1995, AJ, 110, 2622
Lauer, T. R., Faber, S. M., Gebhardt, K., et al. 2005, AJ, 129, 2138
Li, Y.-R., Wang, J.-M., Ho, L. C., Du, P., & Bai, J.-M. 2013, ApJ, 779, 110
Lucy, L. B. 1974, AJ, 79, 745
Maoz, D., & Netzer, H. 1989, MNRAS, 236, 21
Maoz, D., Netzer, H., Leibowitz, E., et al. 1990, ApJ, 351, 75
Menezes, R. B., Steiner, J. E. & Ricci, T. V. 2014, MNRAS, 438, 2597
Netzer, H. 2013, Physics and Evolution of Active Galactic Nuclei (Cambridge: Cambridge Univ. Press)
Osterbrock, D. E. 1989, Astrophysics of gaseous nebulae and active galactic nuclei (Mill Valley, CA: University Science Books)
Osterbrock, D. E., & Mathews, W. G. 1986, ARA&A, 24, 171
Osterbrock, D. E., & Pogge, R. W. 1985, ApJ, 297, 166
Pancoast, A., Brewer, B. J., & Treu, T. 2011, ApJ, 730, 139
Pancoast, A., Brewer, B. J., Treu, T., et al. 2012, ApJ, 754, 49
Pancoast A., Brewer, B. J., & Treu, T. 2014, MNRAS, 445, 3055
Pancoast, A., Brewer, B. J., Treu, T., et al. 2014, MNRAS, 445, 3073
Peterson, B. M., Ali, B., Horne, K., et al. 1993, PASP, 105, 247
Peterson, B. M., Berlind, P., Bertram, R., et al. 2002, ApJ, 581, 197
Peterson, B. M., Ferrarese, L., Gilbert, K. M., et al. 2004, ApJ, 613, 682
Peterson, B. M., Wanders, I., Bertram, R., et al. 1998, ApJ, 501, 82
Rafter, S. E., Kaspi, S., Behar, E., Kollatschny, W., & Zetzl, M. 2011, ApJ, 741, 66
Rafter, S. E., Kaspi, S., Chelouche, D., et al. 2013, ApJ, 773, 24
Rest, A., van den Bosch, F. C., Walter, J., et al. 2001, AJ, 121, 2431
Richardson, W. H. 1972, J. Opt. Soc. Am., 62, 55
Popović, L. Č. 2012, NewAR, 56, 74
Schmidt, M. 1963, Nature, 197, 1040
Schmitt, H. R., & Kinney, A. L. 1996, ApJ, 463, 498
Shen, Y., Horne, K., Grier, C. J., et al. 2015, arXiv:1510.02802
Shen, Y., Richards, G. T., Strauss, M. A., et al. 2011, ApJS, 194, 45
Snyder, D. L., Hammoud, A. M., & White, R. L. 1993, J. Opt. Soc. Am. A, 10, 1014
Sulentic, J. W., Marziani, P., & Dultzin-Hacyan, D. 2000, ARA&A, 38, 521
Trump, J. R., Hall, P. B., Reichard, T. A., et al. 2006, ApJS, 165, 1
Valdes, F., Gupta, R., Rose, J. A., Singh, H. P., & Bell, D. J. 2004, ApJS, 152, 251
Wahlgren, G. M., Leckrone, D. S., Shore, S. N., et al. 1991, ApJL, 377, L41
Wang, J.-M., Du, P., Hu, C., et al. (SEAMBH Collaboration) 2014, ApJ, 793, 108 (Paper II)
Wang, J.-M., Du, P., Valls-Gabaud, D., Hu, C., & Netzer, H. 2013, Phys. Rev. Lett., 110, 081301
White, R. J., & Peterson, B. M. 1994, PASP, 106, 879
Whittle, M. 1992, ApJS, 79, 49